Effect of preferential concentration on turbulent collision rates

Walter C. Reade and Lance R. Collins

Citation: Physics of Fluids **12**, 2530 (2000); doi: 10.1063/1.1288515
View online: http://dx.doi.org/10.1063/1.1288515
View Table of Contents: http://scitation.aip.org/content/aip/journal/pof2/12/10?ver=pdfcov
Published by the AIP Publishing

Effect of preferential concentration on turbulent collision rates

Walter C. Reade[a] and Lance R. Collins[b]
Department of Chemical Engineering, The Pennsylvania State University, University Park, Pennsylvania 16802

(Received 31 August 1998; accepted 16 June 2000)

The effect of particle inertia on the interparticle collision rates of a turbulent aerosol was investigated recently by Sundaram and Collins (1997) using direct numerical simulation (DNS). They observed that for values of the particle Stokes number (here defined as the ratio of the particle response time to Kolmogorov time scale) near unity, the collision frequency was enhanced by between one and two orders of magnitude. This enhancement was attributed in part to the local enrichment of the particle concentration in low-vorticity regions of the flow due to the centrifuge effect commonly referred to as preferential concentration (Eaton and Fessler 1994). Sundaram and Collins (1997) showed that the correction factor for the collision kernel in a preferentially concentrated system is $g(\sigma)$, where $g(r)$ is the particle radial distribution function and σ is the collision diameter. This paper uses DNS, in combination with statistical analysis, to study the dependence of the radial distribution function on the turbulence and particle parameters. A curve fit of the results over a broad range of the relevant dimensionless parameters enables easy estimation of $g(\sigma)$. The effect of system Reynolds number over the limited range accessible by DNS is also presented. In general, the degree of preferential concentration increases with increasing Reynolds number. © *2000 American Institute of Physics.* [S1070-6631(00)51010-1]

I. INTRODUCTION

The dynamical evolution of small particles or droplets embedded in a turbulent flow field continues to receive attention because of its relevance to a broad range of technological and naturally occurring flows. Here we restrict our attention to particle sizes that are small as compared to all of the scales of motion of the fluid and particle volume fractions that are sufficiently small that ''dilute'' conditions prevail, and turbulence modulation[1–3] may be neglected. An important fundamental question that has yet to be satisfactorily addressed is how turbulence affects the interparticle collision rate and ultimately the particle size distribution under conditions that favor coagulation or agglomeration.

An example of a process that is strongly influenced by turbulence-driven coagulation is aerosol production of fine powders.[4–6] The flow in these systems is usually turbulent to enhance the mixing of the reactant species. It is generally accepted that turbulence affects the collision rate between particles and thereby modifies the resulting particle size distribution. Understanding the mechanism by which turbulence enhances the collision rate and its dependence on the system parameters is essential for developing the means to predict and control these aerosol reactors. Similar questions arise in other engineering applications such as sprays, emulsifiers, crystallization reactors, and pneumatic devices. Examples of naturally occurring aerosol systems with similar issues include cloud droplets,[7,8] aerosol transport in the upper atmosphere, and even planet formation from protoplanetary nebula.[9,10] The important features of all of these systems resemble the powder process; however, the enormous range of the Reynolds number in these applications underscores the need for reliable scaling relationships for this parameter.

One of the earliest studies of collision in a turbulent aerosol was by Saffman and Turner[11] who considered the collision rate of inertialess drops that precisely follow fluid streamlines. The collision mechanism they proposed is essentially the same as the one described by von Smoluchowski[12] in laminar shear flows. The collision rate is proportional to a nominal turbulent shear rate, which Saffman and Turner took to be $(\epsilon/\upsilon)^{1/2}$, where υ is the fluid kinematic viscosity and ϵ is the turbulent energy dissipation rate per unit mass of fluid. The functional form of the Saffman–Turner formula is generally accepted, although the assumptions that went into determining the prefactor have been questioned.[13–16]

Abrahamson[17] considered the other limit, namely the collision of particles that have infinite inertia and are completely uncorrelated with the fluid. The collision kernel, derived from kinetic theory arguments, is valid for particles with response times that are long as compared to the fluid time scales. This analysis was extended by Reade and Collins[18] to obtain particle energies and collision rates for the case of a coagulating aerosol.

The collision rate of particles in the intermediate region—where particle response times and fluid time scales are comparable—was originally investigated in the thesis of Balachandar[19] using direct numerical simulation. Balachandar computed the collision rate of finite-size, noninteracting particles in isotropic turbulence and demonstrated the signifi-

[a]Current address: International Paper, 6285 Tri-Ridge Blvd., Loveland, Ohio 45140.
[b]Author to whom correspondence should be addressed. Telephone: 814-863-7113; Fax: 814-865-7846. Electronic mail: LXC12@psu.edu

cance of particle inertia. Although the resolution of the simulations was limited, he correctly surmised that the enhancement in the collision rate is due in part to the large fluctuations in the particle concentration fields that occur with finite-inertia particles. This phenomenon, referred to as ''preferential concentration'' in the literature, results from local vorticity centrifuging particles out of regions of high vorticity into regions of high strain.[20–23] As collision is inherently a nonlinear function of particle concentration, these fluctuations cause a net increase in the overall collision rate. Similar effects have been observed in channel flows,[24,25] especially near the center of the channel, where turbulence is nearly homogeneous and isotropic.

The key parameter identified in all of the previous investigations is the particle Stokes number

$$\mathrm{St}\equiv\frac{\tau_p}{\tau_\eta}=\frac{\frac{1}{18}\left(\frac{\rho_p}{\rho}\right)\frac{\sigma^2}{\upsilon}}{(\upsilon/\epsilon)^{1/2}}=\frac{1}{18}\left(\frac{\rho_p}{\rho}\right)\left(\frac{\sigma}{\eta}\right)^2, \tag{1}$$

where τ_p is the response time of a particle with diameter σ and density ρ_p in a fluid of density ρ, $\tau_\eta\equiv(\upsilon/\epsilon)^{1/2}$ is the Kolmogorov time scale, and $\eta\equiv(\upsilon^3/\epsilon)^{1/4}$ is the Kolmogorov length scale. Preferential concentration is usually observed for particles with $\mathrm{St}\approx 1$. For larger values of the Stokes number [i.e., $\mathrm{St}\approx\sqrt{\mathrm{Re}_\lambda}$, where Re_λ is the turbulent Reynolds number based on the Taylor microscale—see Eq. (14) for the definition], particles become less correlated with the fluid causing the relative velocity between neighboring particles to increase, which results in a higher collision frequency. Both effects are captured by the generalized collision relationship developed by Sundaram and Collins[26]

$$N_c=\frac{1}{2}n^2 4\pi\sigma^2 g(\sigma)\int_{-\infty}^{0}-w_r P(w_r|\sigma)dw_r, \tag{2}$$

where N_c is the number of collisions per unit volume per time, n is the number density of particles, w_r is the radial component of the relative velocity of two particles, $g(r)$ is the radial distribution function (hereafter rdf), and $P(w_r|r)$ is the conditional pdf (probability density function) of the relative velocity of particle pairs along the line of centers conditioned on the separation distance r. [Note, Eq. (2) has been modified to relax the assumption of isotropy of the relative velocity vector in accordance with the subsequent study of Wang *et al.*[27] who showed the assumption to be poor for small-Stokes-number particles.] Sundaram and Collins showed that the preferential concentration mechanism influences the collision frequency through the rdf $g(r)$, whereas the decorrelation of particle motions manifests in the relative velocity pdf $P(w_r|r)$.

The focus of this paper will be on the rdf $g(r)$. As will be shown, collision enhancement due to preferential concentration can be as large as 10–100 fold; thus, accurately estimating $g(\sigma)$ in Eq. (2) is essential to accurately predict N_c. In this study, we consider the behavior of the rdf and its dependence on the system parameters using a large number of direct numerical simulations (DNS). We attempt (wherever possible) to isolate the effect of each parameter. Moreover, we develop a systematic approach to correlate the results from the simulations into a form that allows for easy estimation. The result is suggestive of a possible theoretical framework that one might use to obtain a more rigorous description of the rdf.

We begin by presenting an overview of the DNS algorithm and the parameter values that were explored in Sec. II. Section III then presents simplifications and assumptions used in modeling the rdf. Results for the simpler case of noncolliding (interpenetrating) ''ghost'' particles are then presented in Sec. IV followed by an analysis of elastically rebounding finite-size particles in Sec. V. Section VI shows several sample calculations of $g(r)$ and $g(\sigma)$ for different particle systems. Concluding remarks are given in Sec. VII.

II. DIRECT NUMERICAL SIMULATION

DNS solves the full time-dependent, three-dimensional equations of motion for the fluid and each of the particles. The simulations performed in this study have three facets: (1) simulation of the fluid phase; (2) simulation of particle motion; and, (3) simulation of particle collision. Each will be discussed briefly in the following sections, followed by a short qualitative discussion of preferential concentration.

A. Fluid phase

The fluid phase is governed by the incompressible Navier–Stokes equations. Under the assumption of dilute particle loading, the influence of the particle phase on the turbulence can be neglected (cf. Ref. 1 for a more comprehensive discussion of this point) and the equations of motion reduce to

$$\nabla\cdot\mathbf{u}=0, \tag{3}$$

$$\frac{\partial\mathbf{u}}{\partial t}+\mathbf{u}\cdot\nabla\mathbf{u}=-\frac{1}{\rho}\nabla p+\upsilon\nabla^2\mathbf{u}+\mathbf{F}, \tag{4}$$

where $\mathbf{u}(\mathbf{x},t)$ is the three-dimensional time and space varying velocity field, $p(\mathbf{x},t)$ is the pressure field, ρ and υ are the fluid density and kinematic viscosity respectively, and $\mathbf{F}$ is a forcing function that continuously adds energy to the largest scales of motion.[28] A pseudospectral algorithm[29] was used to update the fluid velocity. Details of the numerical algorithm can be found in Ref. 26.

B. Particle motion

The full equation of motion for particles that are small as compared to the Kolmogorov scale was derived by Maxey and Riley.[30] For dense particles (i.e., $\rho_p/\rho\gg 1$), linear (Stokes) drag is the dominant term, and the equations of motion for the ith particle become

$$\frac{d\mathbf{x}_p^{(i)}}{dt}=\mathbf{v}_p^{(i)}, \tag{5}$$

$$\frac{d\mathbf{v}_p^{(i)}}{dt}=\frac{(\mathbf{u}(\mathbf{x}_p^{(i)})-\mathbf{v}_p^{(i)})}{\tau_p}+\frac{1}{m_p}\sum_{j\neq i}\mathbf{F}^{(ij)}, \tag{6}$$

where $\mathbf{x}_p^{(i)}$ and $\mathbf{v}_p^{(i)}$ are the position and velocity of the centroid of the ith particle, $\mathbf{u}(\mathbf{x}_p^{(i)})$ is the undisturbed fluid ve-

TABLE I. Summary of runs. ''X'' identifies conditions that runs were performed. A single asterisk designates the conditions at which one additional finite-volume run was performed at a nondimensional particle diameter of $\hat{\sigma}=0.175$. A double asterisk designates the conditions at which three additional finite-volume runs were performed at $\hat{\sigma}=0.0875$, 0.175, and 0.35.

St	32^3	64^3	96^3	128^3
0.00		X		
0.05		X		
0.10		X		
0.20	X	X		
0.30		X	X	
0.40		X*		
0.50	X	X*		X
0.60	X	X	X	
0.70	X	X**	X	X
0.80	X	X*		
1.00	X	X**	X	X
1.20			X	
1.50	X	X*	X	
2.00		X		
2.50		X		
3.00		X		
4.00		X		

TABLE II. Turbulence parameters in arbitrary units (with the exception of the final two parameters which are dimensionless). U' is the turbulent energy, ϵ is the dissipation rate, ρ is the fluid density, υ is the kinematic viscosity, L is the integral length scale, T is the integral time scale, η is the Kolmogorov length scale, τ_η is the Kolmogorov time scale, λ is the Taylor microscale, Δt is the time step, Re_λ is the Reynolds number based on the Taylor microscale, and $k_{\max}\eta$ is a measure of the resolution of the simulation.

	32^3	64^3	96^3	128^3
U'	0.82	0.84	0.87	0.91
ϵ	0.22	0.20	0.22	0.25
ρ	1.00	1.00	1.00	1.00
υ	2.2×10^{-2}	1.3×10^{-2}	7.8×10^{-3}	6.3×10^{-3}
L	1.77	1.65	1.54	1.53
T	2.18	1.98	1.77	1.68
η	8.5×10^{-2}	5.6×10^{-2}	3.8×10^{-2}	3.2×10^{-2}
τ_η	0.32	0.25	0.19	0.16
λ	1.01	0.81	0.63	0.57
Δt	3.1×10^{-3}	3.1×10^{-3}	3.1×10^{-3}	3.1×10^{-3}
Re_λ	37.1	54.5	69.7	82.5
$k_{\max}\eta$	1.36	1.80	1.84	2.03

locity at the centroid of the ith particle, $\tau_p \equiv (\rho_p/\rho)\sigma^2/18\upsilon$ is the particle response time, m_p is the mass of the particle, and $\mathbf{F}^{(ij)}$ is the impulse due to an elastic (i.e., momentum and energy conserving) collision between the ith and jth particles. Since particles are not constrained to lie on fluid grid points, it is necessary to interpolate $\mathbf{u}(\mathbf{x}_p^{(i)})$. Details of the third-order Hermitian interpolation scheme used in this study can be found in Ref. 31. Note that zero-St particles are simulated by assigning the instantaneous (interpolated) fluid velocity at the particle center to the particle velocity. Particles obey periodic boundary conditions.

C. Particle collision

When particles of finite size approach to within their collision diameter, a hard-sphere collision is enacted. The detailed algorithm for particle collisions is described in Ref. 31. Note that some of the simulations were performed without checking for collisions. The so-called ghost particles are free to occupy any space in the system without being excluded by other particles.

D. Organization of simulations

The bulk of the simulations for this study were performed on a 64^3 fluid grid. Other simulations were performed on 32^3, 96^3, and 128^3 grids for a total of 32 simulations. Table I details the simulations performed. The various parameters and fluid characteristics of the simulations can be found in Table II. It should be noted that since the simulation is stochastically forced, the instantaneous fluid statistics vary with time; hence, although the particle response time (τ_p) is fixed in a given simulation, the instantaneous particle Stokes number varies slightly throughout the duration of a run, according to Eq. (1).

Each DNS is initialized with a fluid velocity that had previously reached a statistically stationary state. Particles are then randomly placed within the fluid domain and their velocities are initialized with the local fluid velocity. For this reason, it is necessary to let the fluid–particle system run until statistical equilibrium is reached. For all cases, the system is allowed to equilibrate for at least six eddy turnover times, after which the particle positions are recorded at approximately one eddy-turnover-time intervals for a total of eight ''measurements'' during each simulation. Given that there are $N(N-1)/2$ particle pairs in the DNS (more than 3×10^{10} in this case) it is impossible to consider all pairs in each calculation of the rdf. In order to reduce the calculation time, all particle pairs are used to determine the rdf for $r/\eta \leqslant 2.0$ only. For values of r/η larger than 2.0, 25 million particle pairs are selected at random to compute the rdf.

E. Illustration of preferential concentration

Figure 1 shows the dramatic effect that turbulence has on the particle concentration field. The figure shows six $2d$ ''slices'' of the DNS domain (with a thickness of 1/64 the box length) for runs of various St. These slices are taken at the same instant of the DNS, so the underlying flow field is the same for each slice. Figure 1(a) shows a completely homogeneous particle concentration field corresponding to St=0. Figures 1(b)–1(f) show the particle concentration fields at finite St. Notice that as St increases [from approximately 0.2–0.7, corresponding to Figs. 1(b) and 1(c)], the particles increasingly concentrate into low-vorticity regions of the flow. Beyond St=0.7, the particle concentration fields become defocused, as the effect fades away [Figs. 1(d)–1(f)—corresponding to St of 1.0, 2.0, and 4.0, respectively]. The defocusing occurs because particles with too much inertia have difficulty responding to the fluid vorticity fast enough to preferentially concentrate appreciably.

For the 64^3 simulations, there are approximately 112 Kolmogorov lengths (η) to the DNS box. A visual inspection of the concentrated particle fields [Fig. 1, especially Fig.

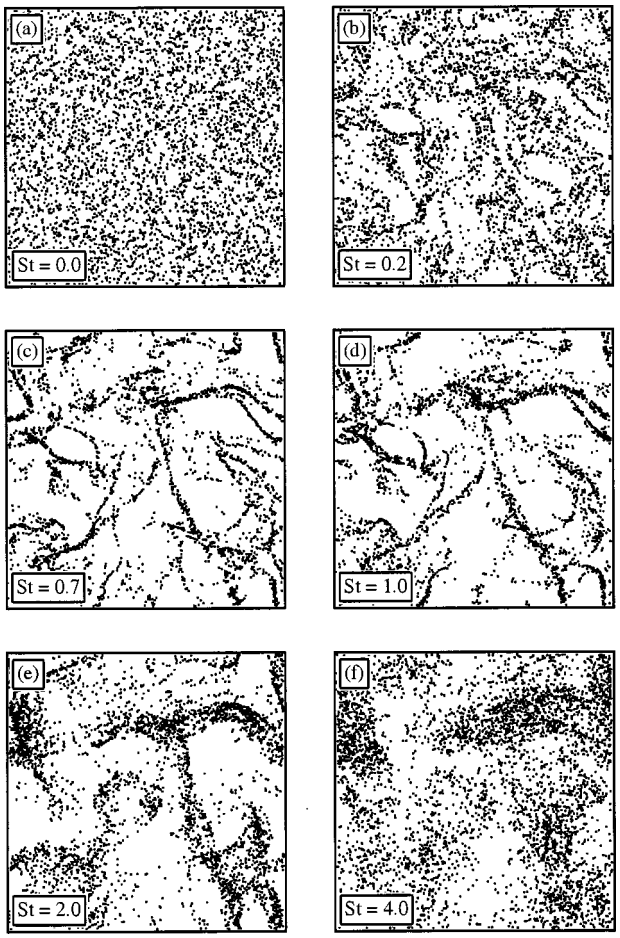

FIG. 1. $2d$ slices of ghost-particle simulations at: (a) St=0.0; (b) St=0.2; (c) St=0.7; (d) St=1.0; (e) St=2.0; and, (f) St=4.0. Dots correspond to particle center locations.

1(c)] suggests that the regions with little or no particles are on the order of 1/10 the box length, making the size of these regions on the order of 10η.

III. MODELING CONSIDERATIONS

A. Radial distribution function

Consider a *canonical* ensemble of systems, each of volume V, containing N indistinguishable particles of diameter, σ, and density, ρ_p. For such an ensemble, the joint probability that each of the N particles lie within volumes $d\mathbf{x}_1$ centered at $\mathbf{x}_1,\ldots,$ through $d\mathbf{x}_N$ centered at $\mathbf{x}_N$ is defined as

$$P^{(N)}(\mathbf{x}_1,\ldots,\mathbf{x}_N)d\mathbf{x}_1\ldots d\mathbf{x}_N, \tag{7}$$

where the standard normalization applies, i.e.,

$$\int_V\cdots\int_V P^{(N)}(\mathbf{x}_1,\ldots,\mathbf{x}_N)d\mathbf{x}_1\cdots d\mathbf{x}_N=1. \tag{8}$$

The two-particle distribution function is then obtained by integrating out the dependence on the remaining particles

$$P^{(2)}(\mathbf{x}_1,\mathbf{x}_2)\equiv\int_V\cdots\int_V P^{(N)}(\mathbf{x}_1,\ldots,\mathbf{x}_N)d\mathbf{x}_3\cdots d\mathbf{x}_N. \tag{9}$$

The two-particle radial distribution function is then defined as[32,33]

$$g(\mathbf{x}_1,\mathbf{x}_2)=\frac{N(N-1)}{n^2}P^{(2)}(\mathbf{x}_1,\mathbf{x}_2), \tag{10}$$

where $n\equiv N/V$. For a statistically homogeneous and isotropic volume, particle positions can be expressed in terms of a relative separation distance, $r\equiv|\mathbf{x}_1-\mathbf{x}_2|$, and $P^{(2)}(\mathbf{x}_1,\mathbf{x}_2)$ reduces to $P^{(2)}(r)/V$ to give the working definition of $g(r)$ used in this study

$$g(r)=\frac{N(N-1)}{n^2V}P^{(2)}(r). \tag{11}$$

As the rdf is near unity for a uniformly distributed system, it is convenient to define a residual rdf (rrdf) as

$$h(r)\equiv g(r)-1. \tag{12}$$

A physical interpretation of $g(r)$ is the number of particle centers located in a spherical shell between r and $r+dr$ about a central particle divided by the expected number of particles given a uniformly distributed particle field. Based on the definition of the rdf shown in Eq. (11) and the integral relationship given in Eq. (8), it is easy to show that the rrdf must satisfy the following integral constraint[34]

$$n\int_V h(r)d\mathbf{r}=-1. \tag{13}$$

B. Parametric dependence

Isotropic turbulence is characterized by the fluid density, ρ, kinematic viscosity, υ, turbulence intensity U', and kinetic energy dissipation rate, ϵ. In dimensionless terms, this reduces to the turbulent Reynolds number, defined here in terms of the Taylor microscale

$$\mathrm{Re}_\lambda\equiv U'^2\sqrt{\frac{15}{\upsilon\epsilon}}. \tag{14}$$

For a monodisperse suspension, the particle phase introduces three additional variables, viz., the particle density ρ_p, diameter σ, and total number N. In terms of dimensionless variables, these can be expressed as the volumetric loading $\alpha\equiv\pi\sigma^3N/6V$, nondimensional size parameter $\hat{\sigma}\equiv\sigma/\eta$ and particle Stokes number St [see Eq. (1)]. This implies that the most general form of the rdf in isotropic turbulence can be expressed functionally as

$$g(\hat{r};\mathrm{Re}_\lambda,\alpha,\hat{\sigma},\mathrm{St}), \tag{15}$$

where $\hat{r}\equiv r/\eta$ is the dimensionless independent variable and the variables after the semicolon are the dimensionless parameters.

C. Simplifying assumptions

The large parameter space shown in Eq. (15) would make it difficult to interpret and correlate the results from the numerical simulations. It is, therefore, advantageous to consider the sensitivity of the rdf to each of the parameters, and search for simplifications where applicable.

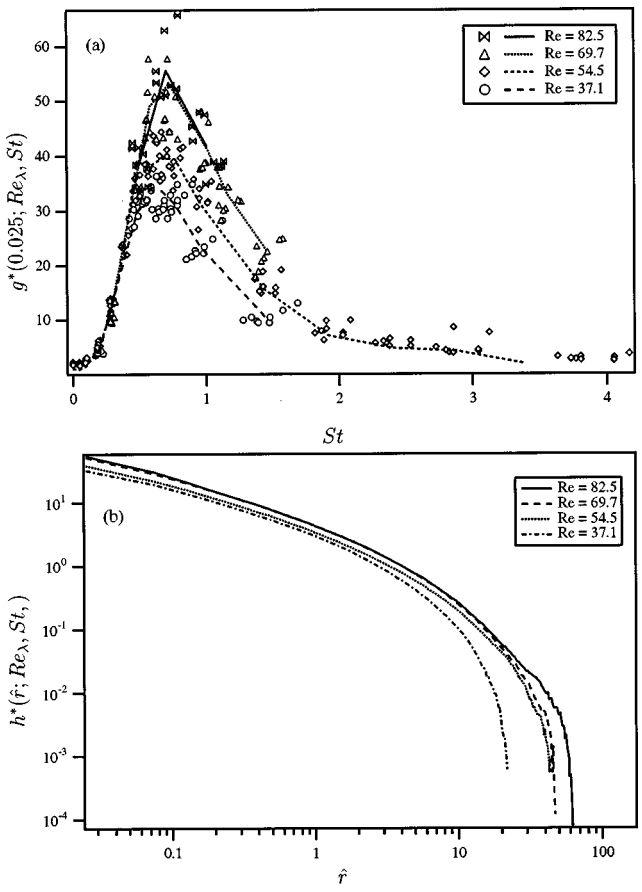

FIG. 2. Effect of Reynolds number (Re_λ) on the radial distribution function of ghost particles. (a) Profiles of $g^*(\hat{r}=0.025;\mathrm{Re}_\lambda,\mathrm{St})$ as a function of Stokes number at the indicated Reynolds numbers. Symbols show individual results for the eight snapshots taken during each run; lines are ensemble averages of the eight snapshots. (b) Profiles of $h^*(\hat{r};\mathrm{Re}_\lambda,\mathrm{St}=1)$ versus $\hat{r}$. The curves shift upwards with increasing Reynolds number.

1. Reynolds number

We begin by considering the dependence on the Reynolds number. Classical scaling arguments, as originally proposed by Kolmogorov,[35] suggest that the small scales should dominate the particle enrichment process since they contain most of the fluid vorticity responsible for centrifuging the particles. The parametric dependence on the small-scale turbulence is accounted for by the Stokes number; thus, the Reynolds number's role is to introduce the effect of the *large* scales on the process. Classical scaling arguments suggest that the large scales should have a vanishingly small role in the limit $\mathrm{Re}_\lambda\to\infty$, i.e., $O(\mathrm{Re}_\lambda^{-p})$, where p is positive.

To test this hypothesis, we performed ghost runs over the range: $37.1\leqslant\mathrm{Re}_\lambda\leqslant 87.5$. (Note, hereafter the superscript* designates a ghost run variable.) Results for the rdf evaluated at $\hat{r}=0.025$ are shown in Fig. 2(a). Notice that the maximum in the curve shifts upward with increasing Reynolds number over the range considered in this study. Similar results were observed in earlier numerical studies.[9,36] The functional dependence on the Reynolds number appears to be separable from the dependence on the other variables. This is apparent in Fig. 2(b), which shows the rrdf versus $\hat{r}$ at several Reynolds numbers. Notice that with increasing Reynolds number the curves mainly shift upward without changing their functional shape substantially. This suggests a decomposition of the form

$$h(\hat{r};\mathrm{Re}_\lambda,\alpha,\hat{\sigma},\mathrm{St})=\Gamma(\mathrm{Re}_\lambda)\tilde{h}(\hat{r};\alpha,\hat{\sigma},\mathrm{St}). \tag{16}$$

Hogan *et al.*[9] attempted to model the Reynolds number dependence of preferential concentration in terms of multifractals. They derived a relationship between the fluctuations in the local particle concentrations and the multi-fractal dimension, $f(\alpha)$. Wang *et al.*[36] were able to collapse their numerical results by assuming a linear proportionality between the rdf and the Reynolds number.

We choose not to speculate on the functional form of $\Gamma(\mathrm{Re}_\lambda)$ at this time. Due to the limited range of Reynolds number in our DNS, it is not possible to distinguish between the various models. For example, the proposal of a linear dependence suggested by Wang *et al.*[36] is certainly plausible, but it might also represent the first term in a Taylor series expansion, in which higher-order terms are still negligible. Given that some applications such as atmospheric turbulence and planetary formation have Reynolds numbers (based on the Taylor microscale) that are two or more orders of magnitude larger than the DNS, there is an essential need to establish the proper scaling relationship for this parameter. However, the question of the Reynolds number dependence will only be answered definitively when DNS or controlled experiments are capable of reaching much higher values than are currently accessible.

The present study focuses on the results for $\mathrm{Re}_\lambda=54.5$. For the sake of simplicity, we set $\Gamma(54.5)=1.0$ and defer any further discussion of this function until a later date. The focus of the remainder of the paper will be on obtaining a correlation for $\tilde{h}(\hat{r};\alpha,\hat{\sigma},\mathrm{St})$.

2. Volume fraction

Earlier studies[1,26] have shown the rdf to be virtually independent of α in the limit $\alpha\to 0$. As we are restricting this study to the dilute limit, we make the assumption

$$\tilde{h}(\hat{r};\alpha\ll 1,\hat{\sigma},\mathrm{St})=\tilde{h}(\hat{r};\hat{\sigma},\mathrm{St}). \tag{17}$$

3. Diameter

The dependence of the rrdf on the particle diameter is found by considering several simulations with particles of different diameter but the same Stokes number. This can be achieved by simultaneously varying the particle diameter and density while holding the product $\rho_p\sigma^2$ fixed. Figure 3 shows the result for three values of $\hat{\sigma}$ and the corresponding ghost run (equivalent to $\hat{\sigma}=0$). Notice that the curves are essentially identical at large $\hat{r}$ and only begin to diverge from each other as $\hat{r}$ approaches $\hat{\sigma}$. This suggests that the ghost particle rrdf provides a good estimate for the hard sphere rrdf for $\hat{r}\gg\hat{\sigma}$; however, for $\hat{r}\approx\hat{\sigma}$ the influence of the collisions causes the two curves to deviate from each other.

This motivates the following decomposition

$$\tilde{h}(\hat{r};\hat{\sigma},\mathrm{St})=\begin{cases} h^*(\hat{r};\mathrm{St})+\Phi(\hat{\sigma},\mathrm{St})f(\overline{r};\mathrm{St}) & \hat{r}\geqslant\hat{\sigma} \\ -1 & \hat{r}<\hat{\sigma} \end{cases}, \tag{18}$$

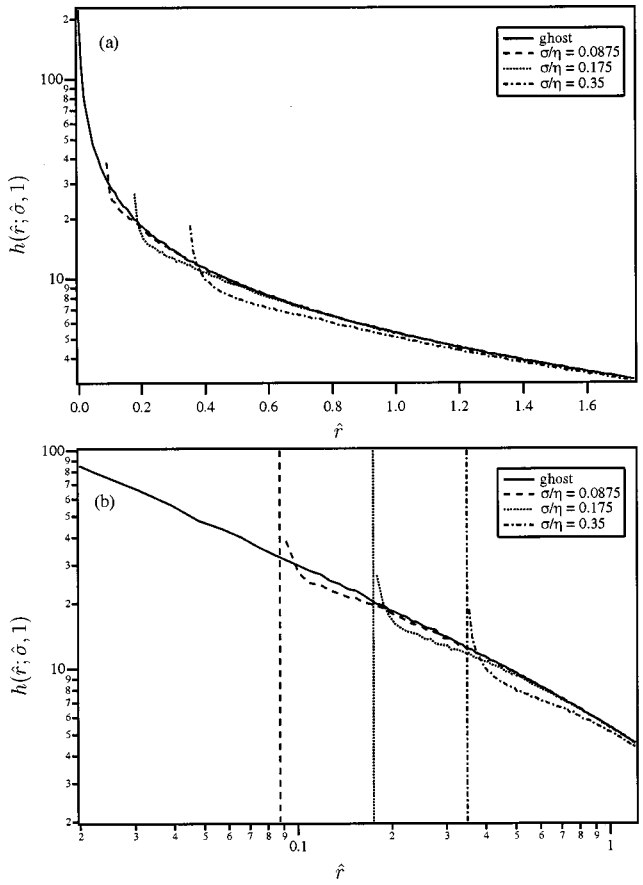

FIG. 3. Residual radial distribution function at St=1.0 for ghost particles (solid line) and finite-volume particles of size $\hat{\sigma}=0.0875$, 0.175, and 0.35 in (a) semilog and (b) logarithmic coordinates. Notice that the curves converge at large $\hat{r}$, however there is a systematic deviation of the finite-volume rrdfs from the ghost as $\hat{r}$ approaches each respective $\hat{\sigma}$.

where $h^*(\hat{r};\mathrm{St})$ is the ghost particle rrdf, $\Phi(\hat{\sigma},\mathrm{St})$ is a normalization factor [see Eq. (20) for its definition], $f(\overline{r};\hat{\sigma},\mathrm{St})$ is a normalized correction function that accounts for finite-size effects [see Eq. (21) for the normalization], and $\overline{r} \equiv r/\sigma$. The decomposition is useful since it allows for a separation of the turbulence–particle interaction—captured by the ghost correlation—from the ''microphysics'' associated with particle collisions—captured by the correction function $f(\overline{r};\hat{\sigma},\mathrm{St})$. It is expected that the turbulence–particle interaction is generic, whereas the microphysical contribution is sensitive to the specific treatment of the collisions. For example, simulations that allow for inelastic collisions, coagulation, or incorporate hydrodynamic, molecular or electrostatic interactions between the particles are likely to yield similar ghost statistics but the correction functions may differ. The present study will consider in some detail the correction function for hard-sphere elastic collisions. Although the result is specific to that case, the general approach can be easily adapted to other circumstances.

As both the ghost and finite-volume rrdf must satisfy the integral constraint expressed in Eq. (13),[32–34] it follows that:

$$\int_V h(r)d\mathbf{r}=\int_V h^*(r)d\mathbf{r}. \tag{19}$$

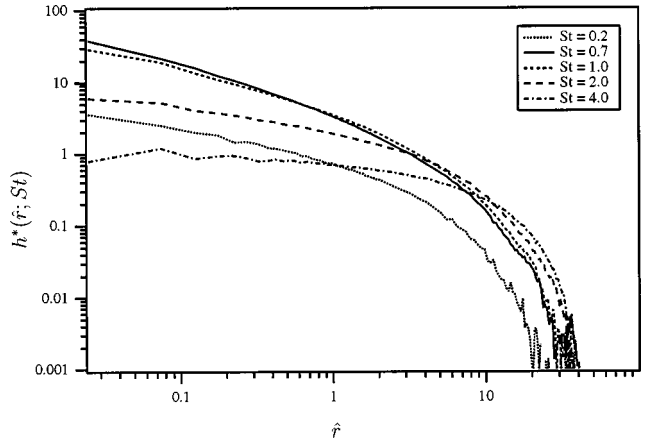

FIG. 4. Residual radial distribution function for the ghost runs corresponding to the slices in Fig. 1 (note the curve corresponding to St=0 is not shown since it is essentially zero except for statistical noise).

Substituting Eq. (18) and simplifying, we arrive at the following constraint for the correction function:

$$\frac{1}{3}+\frac{1}{\hat{\sigma}^3}\int_0^{\hat{\sigma}} h^*(\hat{r})\hat{r}^2 d\hat{r}=\int_1^{\infty}\Phi(\hat{\sigma},\mathrm{St})f(\overline{r})\overline{r}^2 d\overline{r}$$

$$=\Phi(\hat{\sigma},\mathrm{St}), \tag{20}$$

where $f(\overline{r})$ is defined such that

$$\int_1^{\infty} f(\overline{r})\overline{r}^2 d\overline{r}=1. \tag{21}$$

IV. GHOST PARTICLES

Ghost particle simulations were performed on a 64^3 lattice over the range: $0<\mathrm{St}<4$. Figure 4 shows $h^*(\hat{r})$ for the particle fields corresponding to the slices shown in Fig. 1 (the curve for St=0 has been omitted since it is zero to within statistical error). Notice that all of the curves have a similar shape—in all cases a nearly linear (in log–log coordinates) section for small $\hat{r}$ followed by a more rapidly decreasing section at large $\hat{r}$.

This suggests the following functional form for $h^*(\hat{r};\mathrm{St})$

$$h^*(\hat{r};\mathrm{St})=c_0\hat{r}^{-c_1}\exp[-c_2\hat{r}], \tag{22}$$

where c_0, c_1, and c_2 are (in principle) all functions of St. These coefficients—extracted by a least-squares fit of each $h^*(\hat{r};\mathrm{St})$ curve—are plotted in Fig. 5 as a function of St. The values of c_0 show a strong St dependence [Fig. 5(a)], starting near zero at small St, rising to a maximum at St≈0.9, and then decaying as St is increased further. The coefficient c_1 has a similar St dependence, although in this case the peak occurs at St≈0.5 [see Fig. 5(b)]. An empirical fit of these coefficients is given in Table III. Even though c_2 has a similar dependence on St as c_0 and c_1, we have elected to neglect this in the curve fit (i.e., we set $c_2=0.25$ for all Stokes numbers). There are two reasons that drive this decision. First, there is considerably more scatter in this coefficient. Second, this coefficient only affects the curve at large $\hat{r}$, which is of less practical interest. Assigning a constant value

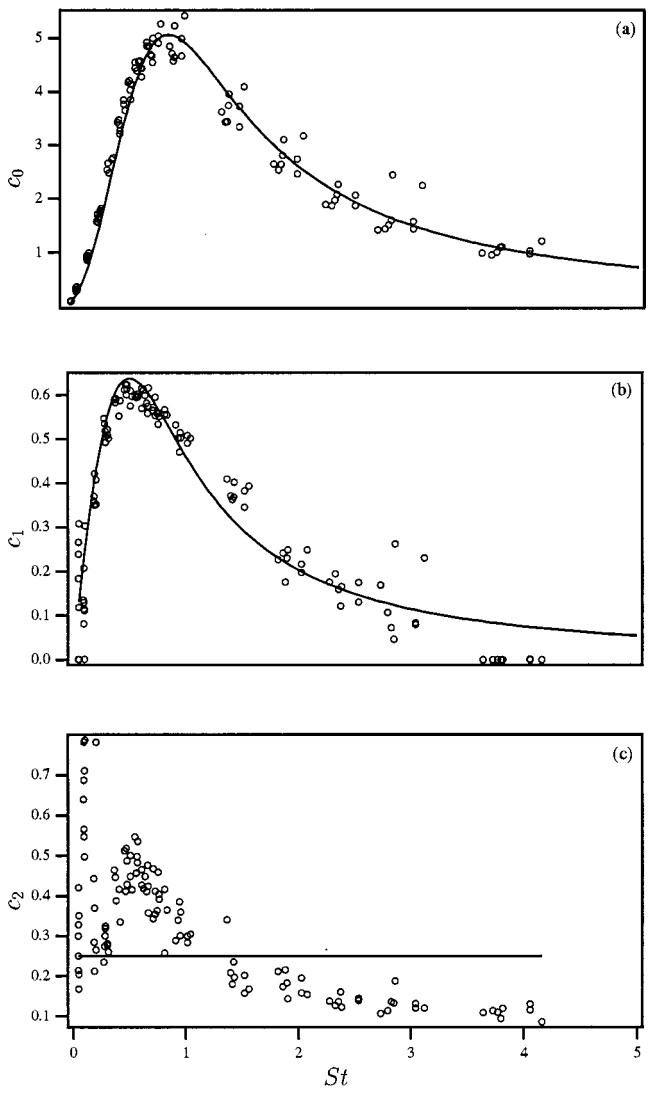

FIG. 5. Coefficients c_0, c_1, and c_2 [see Eq. (22)]—obtained from a curve fit of the DNS results—as a function of Stokes number. The solid line is a curve fit of the coefficients as shown in Table III.

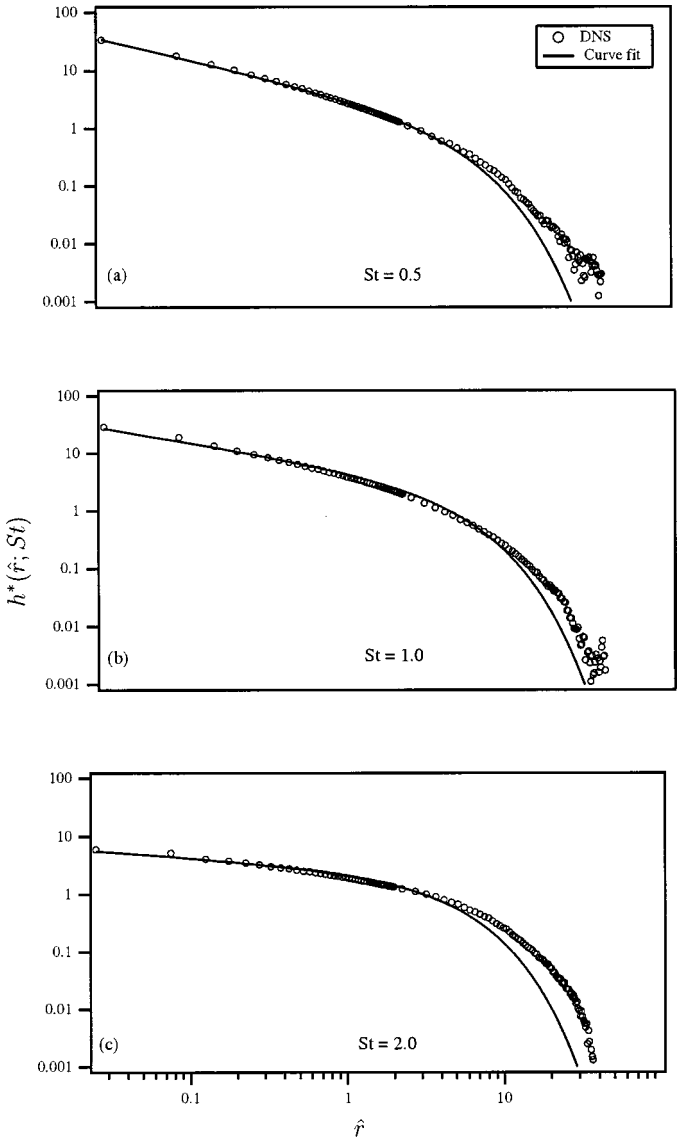

FIG. 6. Comparison of the residual radial distribution function obtained from the DNS with the proposed curve fit at the Stokes numbers indicated on the graphs.

to c_2 does slightly alter the values of the remaining coefficients, but the shape of the rrdf is largely unaffected.

Figure 6 shows a comparison of the curve fit for $h^*(\hat{r};\mathrm{St})$ (solid line) with DNS (open circles) at St of 0.5, 1.0, and 2.0. The curve fit approximates the function well to about $\hat{r}=10$; after this point, the fit decays more rapidly than the DNS. Of course, this could be improved by allowing c_2 to vary with St, but since it is the small values of $\hat{r}$ that are of greatest interest, the present fit is considered to be sufficient.

TABLE III. Coefficients for the correlation of the ghost particle rrdf, $h^*(\hat{r};\mathrm{St})$, given in Eq. (22). The empirical coefficients were obtained by a least-squares minimization of the DNS.

$c_0=\frac{x_0\,\mathrm{St}^{x_1}}{d_0+\mathrm{St}^{x_2}}$	$c_1=\frac{x_3\,\mathrm{St}^{x_4}}{d_1+\mathrm{St}^{x_5}}$	$c_2=0.25$
$x_0=7.92$	$x_3=0.61$	
$x_1=1.80$	$x_4=0.88$	
$x_2=3.29$	$x_5=2.38$	
$d_0=0.58$	$d_1=0.33$	

V. CORRECTION FUNCTION

The correction to the ghost particle correlation involves two functions, $\Phi(\hat{\sigma},\mathrm{St})$ and $f(\overline{r};\mathrm{St})$. $\Phi(\hat{\sigma},\mathrm{St})$ can be evaluated analytically from Eq. (20) by substituting Eq. (22) for $h^*(\hat{r};\mathrm{St})$ and integrating. The result is

$$\Phi(\mathrm{St},\hat{\sigma})=\frac{1}{3}+\frac{c_0 c_2^{(c_1-3)}}{\hat{\sigma}^3}\,\gamma(3-c_1,c_2\hat{\sigma}), \tag{23}$$

where $\gamma(a,b)$ is the incomplete Gamma function defined as[37]

$$\gamma(a,b)\equiv\int_0^b z^{(a-1)}e^{-z}dz.$$

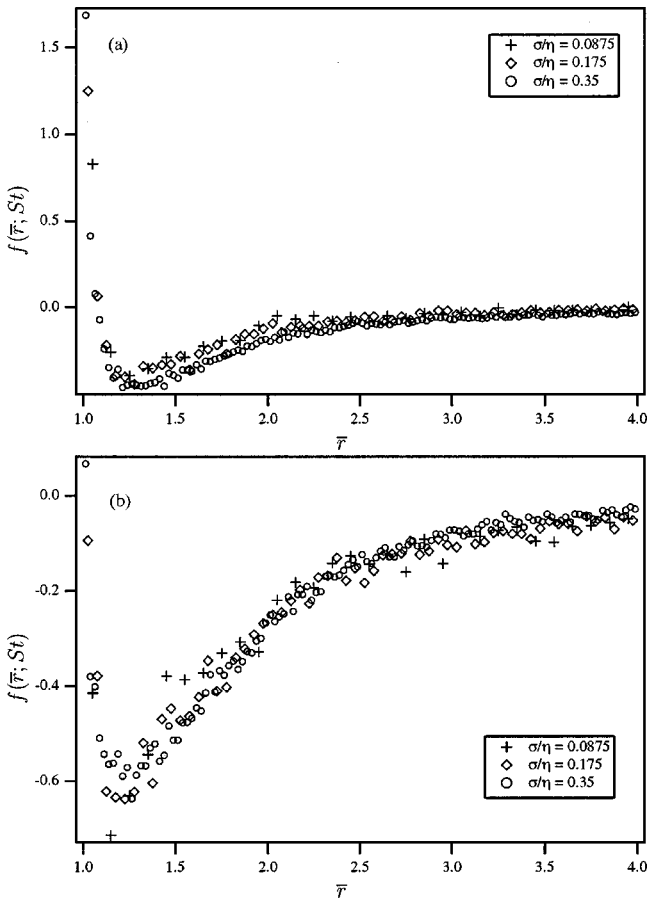

FIG. 7. Correction function, $f(\bar{r};\mathrm{St})$, at (a) St=0.7 and (b) St=1.0. Note that by definition: $\int_1^\infty f(\bar{r})\bar{r}^2 d\bar{r} \equiv 1$.

Recall that the coefficients c_0, c_1, and c_2 are functions of Stokes number (see Table III) and so Φ depends explicitly on the particle size parameter, $\hat{\sigma}$, and implicitly on the Stokes number.

$f(\bar{r};\mathrm{St})$ can be extracted from DNS results for finite-volume particles by evaluating

$$f(\bar{r};\mathrm{St}) = \frac{\tilde{h}(\hat{r};\hat{\sigma},\mathrm{St}) - h^*(\hat{r};\mathrm{St})}{\Phi(\hat{\sigma},\mathrm{St})}. \tag{24}$$

Figure 7 shows $f(\bar{r};\mathrm{St})$ for Stokes numbers of 0.7 and 1.0. The results from different particle diameters appear to collapse onto a single curve in this coordinate, suggesting that the proposed decomposition is reasonable. Notice also that the results for the two Stokes numbers are quantitatively very different.

A. Curve fit

Based on considerations of functional form and asymptotic behavior at small and large Stokes numbers and $\bar{r}$, the following general expression was chosen:

$$f(\bar{r}) = (b_0 - b_1 y)e^{-b_2 y^2} + \frac{b_3 \delta}{\bar{r}^{3+\delta}}, \tag{25}$$

where

$$y \equiv \sqrt{\bar{r} - 1}, \tag{26}$$

TABLE IV. Coefficients for the curve fit for $f(\bar{r};\mathrm{St})$ given in Eq. (25). The empirical coefficients were obtained from a least-squares minimization of the DNS.

b_0	$56.7\times\dfrac{\mathrm{St}^{4/3}(1-0.957\,\mathrm{St})}{(1+19\,\mathrm{St}^{10/3})}$
b_1	$80e^{-4\,\mathrm{St}}$
b_2	$2\,\mathrm{St}^{-5/3}$
b_3	$1-\dfrac{b_0(2+2b_2+b_2^2)}{b_2^3}+\dfrac{\sqrt{\pi}b_1(15+12b_2+4b_2^2)}{8b_2^{7/2}}$

and the coefficients b_0, b_1, b_2, and b_3 are defined in Table IV. The final term on the right-hand side (rhs) of Eq. (25) is added to ensure that the integral constraint given in Eq. (21) is satisfied. Note that the constraint is satisfied for *all* finite values of δ; thus, the effect of this term over any specified range of $\bar{r}$ can be made arbitrarily small by decreasing the value of δ accordingly. For the sake of simplicity, all plots of Eq. (25) suppress this term under the assumption that δ is sufficiently small that its contribution to $f(\bar{r};\mathrm{St})$ is negligible over the range of $\bar{r}$ shown.

The quality of the curve fit is demonstrated in Fig. 8, which shows the fits for particles of size $\hat{\sigma}=0.175$ and Stokes numbers at the two extremes (St=0.4 and St=4.0). It is difficult to achieve the precision observed with the simpler ghost curves; however, Eq. (25) fits all of the runs to within a maximum relative tolerance of 50%. Individual fits vary and most of the errors are much smaller than this maximum tolerance.

VI. IMPACT OF PREFERENTIAL CONCENTRATION ON COLLISION

The complete rdf can now be generated from the following simple expression:

$$g(\hat{r};\mathrm{Re}_\lambda = 54.5, \alpha \ll 1, \hat{\sigma}, \mathrm{St}) = \begin{cases} 1 + h^*(\hat{r};\mathrm{St}) + \Phi(\mathrm{St},\hat{\sigma}) f(\bar{r};\mathrm{St}) & \bar{r} \geqslant 1 \\ 0 & \bar{r} < 1 \end{cases}, \tag{27}$$

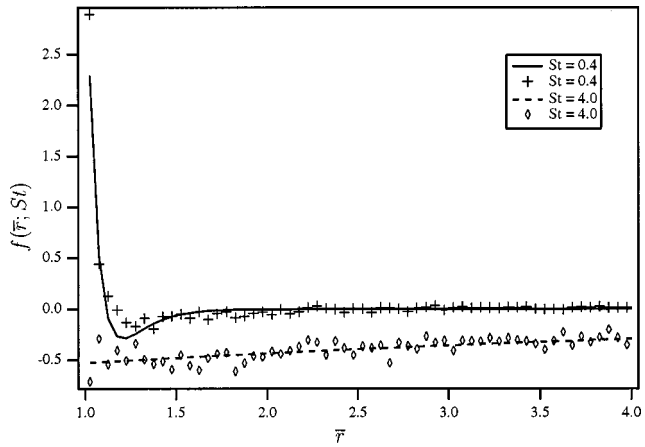

FIG. 8. Comparison of fitted correction function [see Eq. (25)] with DNS at Stokes numbers 0.4 and 4.0 and particle diameter $\hat{\sigma}=0.175$.

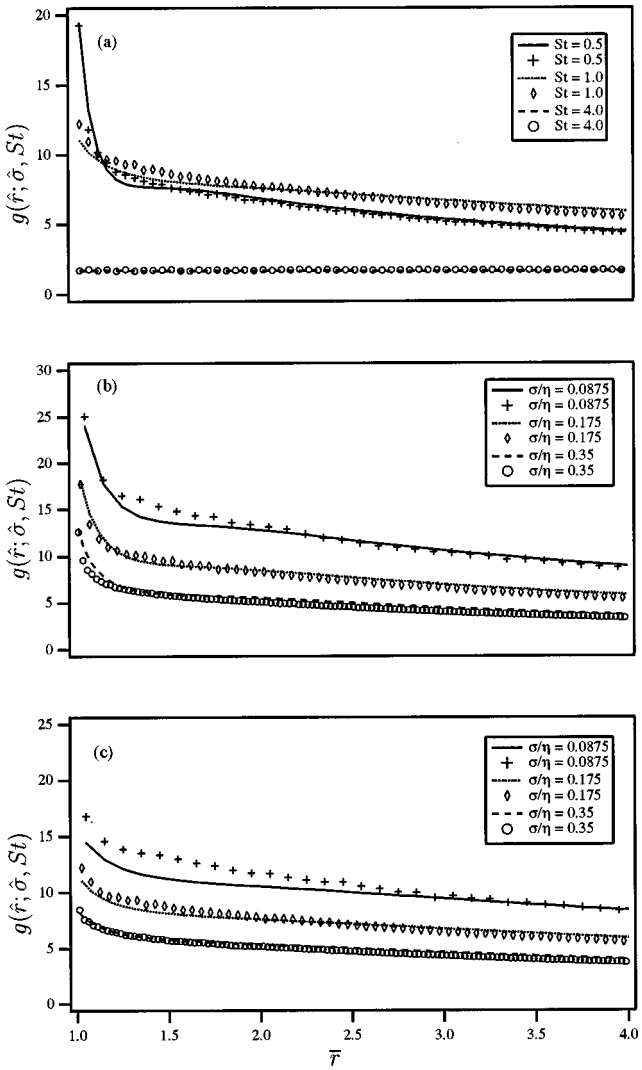

FIG. 9. Comparison of complete curve fit for $g(\hat{r};\hat{\sigma},\mathrm{St})$ with DNS. (a) Dependence on Stokes number (as indicated) at $\hat{\sigma}=0.175$. (b) Dependence on diameter (as indicated) at St=0.7. (c) Dependence on diameter (as indicated) at St=1.0.

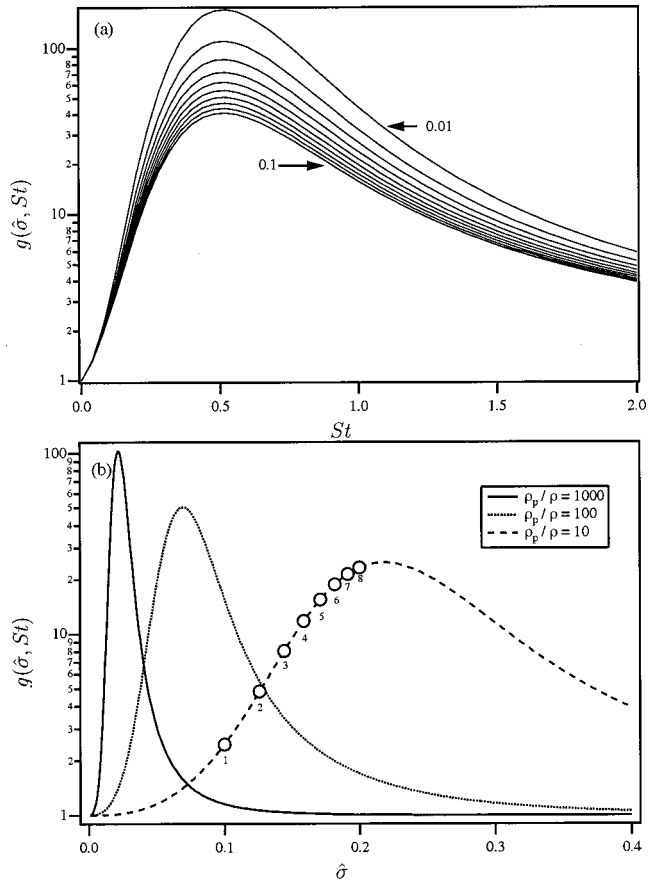

FIG. 10. Collision enhancement factor [i.e., $g(\hat{\sigma},\mathrm{St})$] based on the curve fit. (a) Dependence on Stokes number at particle size parameters: $\hat{\sigma}=0.01,0.02,\ldots,0.1$. Curves corresponding to the extreme values of $\hat{\sigma}$, 0.01 and 0.1, are labeled on the graph. (b) Dependence on particle size parameter at a fixed particle-to-fluid density ratio as indicated on the graph.

where h^*, Φ, and f are given in Eqs. (22), (23), and (25), respectively. Figure 9(a) shows plots of $g(\hat{r};0.175,\mathrm{St})$ (note that we omit the arguments Re_λ and α for the sake of simplicity) at several values of the Stokes number. Figures 9(b) and 9(c) show similar plots at St=0.7 and St=1.0, respectively, and three values of $\hat{\sigma}$. Notice again that the curve fits are good, except at the smallest value of the particle size. There the fit appears to systematically underpredict the value of g. It is believed that the majority of the error arises from the factor Φ.

The goal of this study is to quantify the impact that preferential concentration has on the rate of collisions. Recall that the enhancement factor for the collision kernel is given by the rdf at contact [see Eq. (2)]. According to Eq. (27), this becomes

$$g(\hat{\sigma},\mathrm{St})=1+h^*(\hat{\sigma};\mathrm{St})+\Phi(\mathrm{St},\hat{\sigma})b_0(\mathrm{St}). \tag{28}$$

Notice that this factor depends on the particle Stokes number *and* the dimensionless particle size parameter, $\hat{\sigma}$. Figure 10(a) illustrates the dependence of the enhancement factor on the particle Stokes number with the parameter $\hat{\sigma}$ varied between 0.01 and 0.1. As preferential concentration vanishes in the limits St→0 and St→∞, the enhancement factor approaches unity in both limits. The peak in the factor occurs at approximately St=0.5 for all values of $\hat{\sigma}$. Notice that enhancement factors greater than 100 can be reached under some conditions, highlighting the very strong effect that preferential concentration has on collision frequencies. A less-expected result is that the magnitude of the enhancement factor *increases* with *decreasing* particle size, for fixed Stokes number. The origin of this effect can be traced to the shape of the rdf. To demonstrate this point, it is useful to consider the behavior of Eq. (28) in the limit $\hat{\sigma}\ll 1$ (for fixed Stokes number)

$$\lim_{\hat{\sigma}\to 0} g(\hat{\sigma},\mathrm{St})=\left[1+\frac{b_0(\mathrm{St})}{(3-c_1(\mathrm{St}))}\right]c_0(\mathrm{St})\hat{\sigma}^{-c_1(\mathrm{St})}. \tag{29}$$

We see that for a fixed Stokes number, $g(\hat{\sigma},\mathrm{St})\propto\hat{\sigma}^{-c_1(\mathrm{St})}$, which explains why the collision enhancement factor grows as $\hat{\sigma}$ decreases. Physically, particles are able to pack into a smaller volume as their size decreases. As $g(\hat{\sigma},\mathrm{St})$ is the ratio of the number of neighboring pairs divided by the expected number, its value grows because the expected number vanishes as $\hat{\sigma}\to 0$. Notice that the divergence does not scale

like $\hat{\sigma}^{-3}$, but is slower (i.e., $c_1<3$), suggesting that the numerator is also vanishing, but not fast enough to prevent the divergence of $g(\hat{\sigma},\mathrm{St})$. We conclude that denser (smaller) particles are able to concentrate more, at a given Stokes number, than less dense particles.

A clear illustration of this result is given in Fig. 10(b). The enhancement factor is shown as a function of particle size for density ratios of 10, 100, and 1000. Notice that the peak in the enhancement factor increases and shifts to smaller sizes with increasing particle density. Many aerosol systems have density ratios that are 1000 or greater. In these systems, preferential concentration is likely to play a significant role, even at smaller values of the Stokes number. For example, for particles with a density ratio of 1000, the enhancement factor exceeds 10 at $\hat{\sigma}=0.013$, corresponding to a Stokes number of only 0.17.

A qualitative understanding of the effect that preferential concentration has on the particle size distribution in a *coagulating* aerosol also can be obtained from Fig. 10(b). An illustration of this point is shown for the density ratio of 10 case. An initially monodisperse system of particles of size $\hat{\sigma}=0.02$ (say) will collide and coagulate to produce dimers, trimers, etc. with time. The points on the chart indicate several generations of particles. Notice that each new generation of particles coagulates faster than the parents' generation. Such a trend tends to broaden the particle size distribution at least until the peak in the enhancement factor is reached at $\hat{\sigma}=0.2$. This suggests an important mechanism by which preferential concentration can broaden the particle size distribution of a coagulating aerosol, and may explain the appearance of broad particle size distributions in certain applications (e.g., see Ref. 8 for a detailed discussion of broad droplet spectra in clouds and Ref. 38 for a recent numerical study of coagulating aerosols).

VII. CONCLUDING REMARKS

The influence of preferential concentration on particle collisions has been investigated using direct numerical simulations. Due to the quadratic dependence of the collision frequency on particle concentration, the net effect of preferential concentration is to increase the collision rate above that of a uniform distribution of particles. From the collision formula of Sundaram and Collins,[26] it is known that the enhancement factor for the collision rate is given by $g(\sigma)$, where $g(r)$ is the particle radial distribution function (rdf). Under dilute conditions and in the absence of preferential concentration, this factor is expected to be approximately unity. For strongly concentrated systems, it can reach values that exceed 100.

A systematic analysis of the rdf has been undertaken in order to understand its dependence on the system parameters. It is argued that under dilute conditions, its dependence on the system loading may be neglected. The dependence of the rdf on the Reynolds number was separated from its dependence on the other parameters, allowing us to define a single factor $\Gamma(\mathrm{Re}_\lambda)$ that accounts for the Reynolds number. However, we do not speculate on the functional form of $\Gamma(\mathrm{Re}_\lambda)$ due to the limited range of the Reynolds number achieved in the present DNS. We anticipate that a complete understanding of this parameter requires a combination of higher-resolution DNS, high-Reynolds-number experiments and modern scaling laws that take into account turbulence intermittency.[39]

The dependence of the rdf on the Stokes number and diameter was explored. A decomposition of the rdf into a turbulence-dependent function [the ghost rdf, $h^*(\hat{r};\mathrm{St})$] and a microphysical correction [$\Phi(\hat{\sigma},\mathrm{St})f(\overline{r};\mathrm{St})$] was proposed to facilitate the modeling. The ghost rrdf—found by eliminating particle collisions in the DNS—depends on the Stokes number, but not the particle diameter. At small $\hat{r}$, the ghost rdf has a power-law dependence of the form $\hat{r}^{-c_1}$, where integrability requires that $c_1<3$. At larger $\hat{r}$ the power-law gives way to an exponential tail, suggesting that the ghost rrdf function takes the general form $h^*(\hat{r};\mathrm{St})=c_0\hat{r}^{-c_1}e^{-\hat{r}/4}$, where the coefficients c_0 and c_1 are given in Table III.

The correction function for elastically rebounding hard spheres in the absence of hydrodynamic interactions takes the form $\Phi(\hat{\sigma},\mathrm{St})f(\overline{r};\mathrm{St})$. The integral constraint given in Eq. (21) allowed us to obtain a closed form expression for $\Phi(\hat{\sigma},\mathrm{St})$. The model for $f(\overline{r};\mathrm{St})$ is $(b_0-b_1y)e^{-b_2y^2}+b_3\delta/\overline{r}^{3+\delta}$, where $y=\sqrt{\overline{r}-1}$ and the coefficients b_0, b_1, b_2, and b_3 are given in Table IV. It is important to emphasize that the correction function depends on the microphysics; thus, changes in the treatment of the near-contact motion of particles such as the inclusion of hydrodynamic and/or molecular interactions, inelastic collisions, coagulation, etc. may change the correction function. Nevertheless, the approach outlined here can be easily extended to these other circumstances.

The combination of the ghost and correction rdfs enables an easy estimation of ''enhancement factors'' for the collision kernel. The factors are strong functions of the particle Stokes number *and* the size parameter, $\hat{\sigma}$. The latter dependence can be thought of, alternatively, as a dependence on the particle-to-fluid density ratio. More dense particles (at a given Stokes number) are able to concentrate more strongly and thus achieve higher enhancement factors. Physically, smaller particles are able to pack more tightly into the concentrated regions, thus allowing for greater superpopulations at small separations. The sensitive dependence of preferential concentration on the particle Stokes number has been reported in several earlier studies; however, the importance of the size parameter is only now coming to light. The reason is that most earlier work focused on point-mass particles[20–23,40] or particles of fixed size[36] and so they did not fully explore this parameter. Its role in aerosols with density ratios that exceed 1000 may be significant.

Finally, a qualitative picture of how preferential concentration influences the particle size distribution of a coagulating aerosol has been discussed. For small particles, it is anticipated that the degree of preferential concentration will *increase* with each subsequent generation (dimer, trimer, etc.), implying there is effectively a higher-order dependence of the collision kernel on the diameter. Such a dependence tends to broaden the particle size distribution. Indeed, the

present results appear to qualitatively explain tails in the particle size distribution that we observed numerically in a separate study of coagulating particles.[38]

ACKNOWLEDGMENTS

The authors gratefully acknowledge financial support from the National Science Foundation, Grant No. CTS-9417527. All computations were performed on IBM SP2 nodes that were provided by generous support from the IBM Shared University Research (SUR) program.

[1]S. Sundaram and L. R. Collins, ''A numerical study of the modulation of isotropic turbulence by suspended particles,'' J. Fluid Mech. **379**, 105 (1999).
[2]S. E. Elghobashi and G. C. Truesdell, ''On the two-way interaction between homogeneous turbulence and dispersed particles. I: Turbulence modification,'' Phys. Fluids A **5**, 1790 (1993).
[3]K. D. Squires and J. K. Eaton, ''Particle response and turbulence modification in isotropic turbulence,'' Phys. Fluids A **2**, 1191 (1990).
[4]S. E. Pratsinis and P. T. Spicer, ''Competition between gas phase and surface oxidation of $TiCl_4$ during synthesis of TiO_2 particles,'' Chem. Eng. Sci. **53**, 1861 (1998).
[5]Y. Xiong and S. E. Pratsinis, ''Gas phase production of particles in reactive turbulent flows,'' J. Aerosol Sci. **22**, 637 (1991).
[6]J. D. Landgrebe and S. E. Pratsinis, ''Gas-phase manufacture of particulates: Interplay of chemical reaction and aerosol coagulation in the free-molecular regime,'' Ind. Eng. Chem. Res. **28**, 1474 (1989).
[7]M. B. Pinsky and A. P. Khain, ''Turbulence effects on droplet growth and size distribution in clouds—A review,'' J. Aerosol Sci. **28**, 1177 (1997).
[8]R. A. Shaw, W. C. Reade, L. R. Collins, and J. Verlinde, ''Preferential concentration of cloud droplets by turbulence: Effects on the early evolution of cumulus cloud droplet spectra,'' J. Atmos. Sci. **55**, 1965 (1998).
[9]R. C. Hogan, J. N. Cuzzi, and A. R. Dobrovolskis, ''Scaling properties of particle density fields formed in simulated turbulent flows,'' Phys. Rev. E **60**, 1674 (1999).
[10]J. N. Cuzzi, A. R. Dobrovolskis, and R. C. Hogan, *Chondrules and the Protoplanetary Disk*, Chapter Turbulence, Chondrules, and Planetesimals (Cambridge University, Cambridge, 1996).
[11]P. G. Saffman and J. S. Turner, ''On the collision of drops in turbulent clouds,'' J. Fluid Mech. **1**, 16 (1956).
[12]M. Smoluchowski, ''Versuch einer mathematischen theorie der koagulationskinetic kolloider losungen,'' Z. Phys. Chem., Stoechiom. Verwandtschaftsl. **92**, 129 (1917).
[13]L.-P. Wang, A. S. Wexler, and Y. Zhou, ''On the collision rate of small particles in isotropic turbulence. I. Zero-inertia case,'' Phys. Fluids **10**, 266 (1998).
[14]B. K. Brunk, D. L. Koch, and L. W. Lion, ''Hydrodynamic pair diffusion in isotropic random velocity fields with application to turbulent coagulation,'' Phys. Fluids **9**, 2670 (1997).
[15]B. K. Brunk, D. L. Koch, and L. W. Lion, ''Turbulent coagulation of colloidal particles,'' J. Fluid Mech. **364**, 81 (1998).
[16]B. K. Brunk, D. L. Koch, and L. W. Lion, ''Observations of coagulation in isotropic turbulence,'' J. Fluid Mech. **371**, 81 (1998).
[17]J. Abrahamson, ''Collision rates of small particles in a vigorously turbulent fluid,'' Chem. Eng. Sci. **30**, 1371 (1975).
[18]W. C. Reade and L. R. Collins, ''Collision and coagulation in the infinite-Stokes-number regime,'' Aerosol. Sci. Technol. **29**, 493 (1998).
[19]S. Balachandar, ''Particle coagulation in homogeneous turbulence,'' Ph.D. thesis, Brown University, 1988.
[20]M. R. Maxey, ''The gravitational settling of aerosol particles in homogeneous turbulence and random flow fields,'' J. Fluid Mech. **174**, 441 (1987).
[21]K. D. Squires and J. K. Eaton, ''Preferential concentration of particles by turbulence,'' Phys. Fluids A **3**, 1169 (1991).
[22]L. P. Wang and M. R. Maxey, ''Settling velocity and concentration distribution of heavy particles in homogeneous isotropic turbulence,'' J. Fluid Mech. **256**, 27 (1993).
[23]J. K. Eaton and J. R. Fessler, ''Preferential concentration of particles by turbulence,'' Int. J. Multiphase Flow **20**, 169 (1994).
[24]M. Chen, K. Kontomaris, and J. B. McLaughlin, ''Direct numerical simulation of droplet collisions in a turbulent channel flow part I: Collision algorithm,'' Int. J. Multiphase Flow **24**, 1079 (1998).
[25]M. Chen, K. Kontomaris, and J. B. McLaughlin, ''Direct numerical simulation of droplet collisions in a turbulent channel flow part II: Collision rates,'' Int. J. Multiphase Flow **24**, 1105 (1998).
[26]S. Sundaram and L. R. Collins, ''Collision statistics in an isotropic, particle-laden turbulent suspension I. Direct Numerical Simulations,'' J. Fluid Mech. **335**, 75 (1997).
[27]L.-P. Wang, A. S. Wexler, and Y. Zhou, ''Statistical mechanical descriptions of turbulent coagulation,'' Phys. Fluids **10**, 2647 (1998).
[28]V. Eswaran and S. B. Pope, ''An examination of forcing in direct numerical simulations of turbulence,'' Comput. Fluids **16**, 257 (1988).
[29]C. Canuto, M. Y. Hussaini, A. Quarteroni, and T. A. Zang, *Spectral Methods in Fluid Dynamics* (Springer-Verlag, New York, 1988).
[30]M. R. Maxey and J. J. Riley, ''Equation of motion for a small rigid sphere in a nonuniform flow,'' Phys. Fluids A **26**, 883 (1983).
[31]S. Sundaram and L. R. Collins, ''Numerical considerations in simulating a turbulent suspension of finite-volume particles,'' J. Comput. Phys. **124**, 337 (1996).
[32]T. L. Hill, *Statistical Thermodynamics* (Addison-Wesley, Menlo Park, 1960).
[33]D. A. McQuarrie, *Statistical Mechanics* (Harper & Row, New York, 1976).
[34]T. L. Hill, *Statistical Mechanics: Principles and Selected Applications* (McGraw-Hill, New York, 1956).
[35]A. N. Kolmogorov, ''The local structure of turbulence in an incompressible viscous fluid for very large Reynolds numbers,'' Dokl. Akad. Nauk SSSR **30**, 299 (1941).
[36]L.-P. Wang, A. S. Wexler, and Y. Zhou, ''Statistical mechanical description and modeling of turbulent collision of inertial particles,'' J. Fluid Mech. **415**, 117 (2000).
[37]M. Abramowitz and I. A. Stegun, *Handbook of Mathematical Functions* (Dover, New York, 1964).
[38]W. C. Reade and L. R. Collins, ''A numerical study of the particle size distribution of an aerosol undergoing turbulent coagulation,'' J. Fluid Mech. **415**, 45 (2000).
[39]K. R. Sreenivasan and R. A. Antonia, ''The phenomenology of small-scale turbulence,'' Annu. Rev. Fluid Mech. **29**, 435 (1997).
[40]J. B. McLaughlin, ''Numerical computation of particles-turbulence interaction,'' Int. J. Multiphase Flow **20**, 211 (1994).